INTERNATIONAL JOURNAL FOR NUMERICAL METHODS IN FLUIDS, VOL. 6, 861–882 (1986)

# THREE-DIMENSIONAL ANALYSIS OF THE FLOW IN A CURVED HYDRAULIC TURBINE DRAFT TUBE

WEI SHYY AND MARK E. BRAATEN

*General Electric Corporate Research and Development, PO Box 8, Schenectady, New York 12301, U.S.A.*

## SUMMARY

The three-dimensional turbulent flow in a curved hydraulic turbine draft tube is studied numerically. The analysis is based on the steady Reynolds-averaged Navier–Stokes equations closed with the $k$–$\varepsilon$ model. The governing equations are discretized by a conservative finite volume formulation on a non-orthogonal body-fitted co-ordinate system. Two grid systems, one with $34 \times 16 \times 12$ nodes and another with $50 \times 30 \times 22$ nodes, have been used and the results from them are compared. In terms of computing effort, the number of iterations needed to yield the same degree of convergence is found to be proportional to the square root of the total number of nodes employed, which is consistent with an earlier study made for two-dimensional flows using the same algorithm. Calculations have been performed over a wide range of inlet swirl, using both the hybrid and second-order upwind schemes on coarse and fine grids. The addition of inlet swirl is found to eliminate the stalling characteristics in the downstream region and modify the behaviour of the flow markedly in the elbow region, thereby affecting the overall pressure recovery noticeably. The recovery factor increases up to a swirl ratio of about 0·75, and then drops off. Although the general trends obtained with both finite difference operators are in agreement, the quantitative values as well as some of the fine flow structures can differ. Many of the detailed features observed on the fine grid system are smeared out on the coarse grid system, pointing out the necessity of both a good finite difference operator and a good grid distribution for an accurate result.

KEY WORDS Three Dimensional Flow Turbine Draft Tube Curvilinear Co-ordinates

## INTRODUCTION

The efficiency and power output of a hydraulic turbine used to generate electrical power are significantly affected by the performance of its draft tube. As shown in Figure 1, the draft tube is a curved diffuser located beneath the turbine that delivers the exhaust flow from the turbine to the tailwater basin. The role of the draft tube is to reduce the velocity of the water exiting from the turbine, thereby converting the excess kinetic energy of the exhaust stream into a rise in static pressure. Since the velocity head recovered by the draft tube represents a sizeable fraction of the total effective head on the turbine, it is important for good turbine performance that the draft tube have a high-pressure recovery factor.

For a number of reasons, the proper design of a draft tube is a difficult task. The geometry of a typical draft tube is complicated, as illustrated in Figures 2 and 3. It consists essentially of a short conical diffuser followed by a 90° elbow of varying cross-section and then a rectangular diffuser section. The shape of the cross-section changes from being circular at the inlet end, to elliptical within the elbow, and finally to rectangular at the exit. At the same time, the cross-sectional area of the tube increases from inlet to outlet. This complicated geometry is hard to characterize and it makes analysis difficult.

The flow in a diffuser is characterized by a number of regimes, as described in Reference 1, including (1) a region of well-behaved and unseparated flow and (2) a region of large transitory stall. The point of optimum pressure recovery often falls just within the region of transitory stall, in

0271–2091/86/120861–22$11.00

*Received 2 February 1986*
*Revised 18 April 1986*

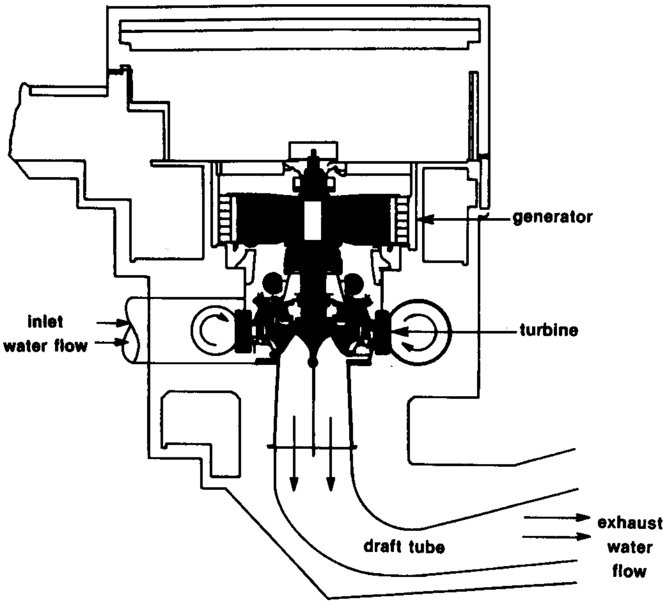

Figure 1. The draft tube of a hydroelectric turbine

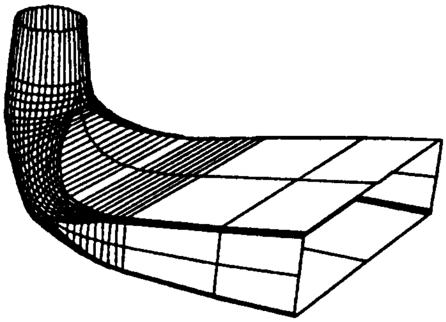

Figure 2. Three-dimensional view of a hydraulic turbine draft tube

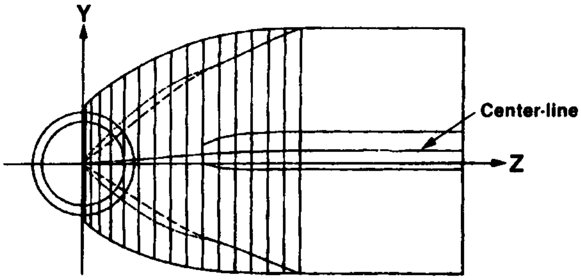

Figure 3. Top view of the draft tube

which the flow is both three-dimensional and transient. The demarcation between the different flow regimes depends on many factors, including the area ratio, the aspect ratio and inlet swirl.

Another complicating factor is that the flow supplied to the draft tube from the turbine is highly non-uniform, turbulent and swirling. Since the pressure recovery factor is sensitive to the specific inlet conditions, they must be accounted for in the analysis.

## PREVIOUS STUDIES

Because of the complex nature of the flow, most diffuser studies have been of an experimental nature. Japikse[2] has prepared a comprehensive survey of the diffuser literature up to 1984, which includes the principal results of many of these studies. There is little information in the open literature directly related to draft tubes of the type studied here, and almost none of a fundamental nature. Some practical guidelines as to the optimum dimensions for such draft tubes are given in Reference (3). In that work it is noted that significant variations in the design of draft tubes with similar external dimensions are common, and that many times the final design is dictated by considerations other than the fluid mechanics.

A number of more fundamental studies relating to individual aspects of the draft tube problem have been reported. The flow in simple curved diffusers of various cross-sections has been studied experimentally.[4,5] The performance of a curved diffuser was found to be invariably poorer than for a comparable straight diffuser with the same area ratio and aspect ratio. The effects of swirling inlet flows have been studied for straight centreline conical diffusers.[6] Swirl was found to improve the pressure recovery significantly for diffusers in which the flow was moderately or badly stalled, but to have little effect on diffusers in which the flow was unseparated.

The analysis of flows in curved ducts of constant cross-sectional area has received more attention, and a number of numerical studies have been performed.[7,8] In such cases, the analysis is simpler since the flow has a predominant direction, and the three-dimensional parabolic form of the Navier–Stokes equations can be solved. The computer storage and time required to solve the parabolized equations are substantially less than those for solving the fully elliptic form of the equations. The results of the published studies show that the curvature of the duct leads to centrifugal forces that set up secondary flows and significantly distort the velocity profiles relative to those in a straight duct.

Recently, some attempts have been made to calculate flows in various diffuser geometries and in curved ducts of complex shape. Hah[9] investigated the effects of inlet swirl and distortion on flows in planar, conical and annular diffusers using a two-dimensional planar or axisymmetric finite difference formulation. Reggio and Camarero[10] computed the flow in a twisted elbow using a three-dimensional curvilinear co-ordinate system. Although the elbow considered appeared to have a constant cross-sectional area, its twisted nature made the flow fully three-dimensional and elliptic in nature. Shyy[11,12] conducted a study of flow in an axisymmetric dump diffuser with two branches. The outflow boundary conditions, and their interactions with the grid system, finite difference operators and computing efficiencies were investigated.

## MODEL FORMULATION

The physical model of the flow in the draft tube is based on the Reynolds-averaged Navier–Stokes equations plus an appropriate turbulence model. The equations are expressed in their three-dimensional fully elliptic form to allow for the possibility of streamwise flow recirculation caused by the changing cross-sectional area of the draft tube. Since the working fluid is water, the incompressible forms of the equations are used.

To keep the computational costs from becoming prohibitive, the flow is assumed to be steady. Since transitory stall is more likely at high divergence angles and at large ratios of diffuser length to width, the present analysis is strictly valid only for relatively short draft tubes with small divergence angles. As mentioned earlier, the demarcation of the line of first appreciable stall is difficult because it depends on many factors. Since its analytical determination would require the solution of the transient, three-dimensional, fully elliptic form of the Reynolds-averaged Navier–Stokes equations, which at present is still impractical because of the vast computer resources that would be required, this must still be done experimentally. Although the optimum pressure recovery often occurs slightly above the line of first appreciable stall, the results from the steady-state model for a diffuser operating just below the line of first appreciable stall are expected to be quite similar, and to provide a good starting point for a final design.

The standard $k$–$\varepsilon$ turbulence model[13] is adopted, along with the wall function treatment for the near wall regions. Although the $k$–$\varepsilon$ model performs well in many flows, it is known to have deficiencies in flows with strong streamline curvature[14] and also in strongly swirling flows.[15] A number of modifications have been proposed in an attempt to overcome these deficiencies,[14–16] including changing the values of the constants in the standard model, adding additional terms to account for streamwise curvature and swirl, and the use of the algebraic stress model or the second moment closure model. However, it appears that more work is needed to demonstrate the universality of these modifications, especially in the context of three-dimensional flows.

## NUMERICAL ALGORITHM

The numerical procedure used to solve the three-dimensional fully elliptic form of the governing conservation equations is an outgrowth of the two-dimensional procedure described in References 17 and 18.

The governing equations are written in the strong conservation law form in general curvilinear co-ordinates, as derived by Vinokur.[19] The conservation equations can typically be written in Cartesian co-ordinates for the dependent variable $\phi$ in the following form:

$$\frac{\partial}{\partial x}(\rho u\phi)+\frac{\partial}{\partial y}(\rho v\phi)+\frac{\partial}{\partial y}(\rho w\phi)=\frac{\partial}{\partial x}\left(\Gamma\frac{\partial\phi}{\partial x}\right)+\frac{\partial}{\partial y}\left(\Gamma\frac{\partial\phi}{\partial y}\right)+\frac{\partial}{\partial z}\left(\Gamma\frac{\partial\phi}{\partial z}\right)+R(x,y,z), \tag{1}$$

where $\Gamma$ is the effective diffusion coefficient and $R$ is the source term. When new independent variables $\xi, \eta$ and $\gamma$ are introduced, equation (1) changes according to the general transformation $\xi=\xi(x,y,z), \eta=\eta(x,y,z), \gamma=\gamma(x,y,z)$. The result of this co-ordinate transformation is to transform the arbitrarily shaped physical domain into a rectangular parallelepiped.

Equation (1) can be rewritten in $(\xi,\eta,\gamma)$ co-ordinates as follows:

$$\begin{aligned}\frac{\partial}{\partial\xi}(\rho U\phi)+\frac{\partial}{\partial\eta}(\rho V\phi)+\frac{\partial}{\partial\gamma}(\rho W\phi)&\\ =\frac{\partial}{\partial\xi}\left[\frac{\Gamma}{J}(q_{11}\phi_\xi+q_{12}\phi_\eta+q_{13}\phi_\gamma)\right]&\\ +\frac{\partial}{\partial\eta}\left[\frac{\Gamma}{J}(q_{21}\phi_\xi+q_{22}\phi_\eta+q_{23}\phi_\gamma)\right]&\\ +\frac{\partial}{\partial\gamma}\left[\frac{\Gamma}{J}(q_{31}\phi_\xi+q_{32}\phi_\eta+q_{33}\phi_\gamma)\right]&+S(\xi,\eta,\gamma)J,\end{aligned} \tag{2}$$

where

$$
\begin{aligned}
U &= u(y_\eta z_\gamma - y_\gamma z_\eta) + v(x_\gamma z_\eta - x_\eta z_\gamma) + w(x_\eta y_\gamma - x_\gamma y_\eta),\\
V &= u(y_\gamma z_\xi - y_\xi z_\gamma) + v(x_\xi z_\gamma - x_\gamma z_\xi) + w(x_\gamma y_\xi - x_\xi y_\gamma),\\
W &= u(y_\xi z_\eta - y_\eta z_\xi) + v(x_\eta z_\xi - x_\xi z_\eta) + w(x_\xi y_\eta - x_\eta y_\xi),\\
q_{11} &= (y_\eta z_\gamma - y_\gamma z_\eta)^2 + (x_\gamma z_\eta - x_\eta z_\gamma)^2 + (x_\eta y_\gamma - x_\gamma y_\eta)^2,\\
q_{22} &= (y_\gamma z_\xi - y_\xi z_\gamma)^2 + (x_\xi z_\gamma - x_\gamma z_\xi)^2 + (x_\gamma y_\xi - x_\xi y_\gamma)^2,\\
q_{33} &= (y_\xi z_\eta - y_\eta z_\xi)^2 + (x_\eta z_\xi - x_\xi z_\eta)^2 + (x_\xi y_\eta - x_\eta y_\xi)^2,\\
q_{12} &= q_{21} = (y_\gamma z_\xi - y_\xi z_\gamma)(y_\eta z_\gamma - y_\gamma z_\eta) + (x_\xi z_\gamma - x_\gamma z_\xi)(x_\gamma z_\eta - x_\eta z_\gamma)\\
&\qquad + (x_\gamma y_\xi - x_\xi y_\gamma)(x_\eta y_\gamma - x_\gamma y_\eta),\\
q_{13} &= q_{31} = (y_\xi z_\eta - y_\eta z_\xi)(y_\eta z_\gamma - y_\gamma z_\eta) + (x_\gamma z_\eta - x_\eta z_\gamma)(x_\eta z_\xi - x_\xi z_\eta)\\
&\qquad + (x_\xi y_\eta - x_\eta y_\xi)(x_\eta y_\gamma - x_\gamma y_\eta),\\
q_{23} &= q_{32} = (y_\xi z_\eta - y_\eta z_\xi)(y_\gamma z_\xi - y_\xi z_\gamma) + (x_\eta z_\xi - x_\xi z_\eta)(x_\xi z_\gamma - x_\gamma z_\xi)\\
&\qquad + (x_\xi y_\eta - x_\eta y_\xi)(x_\gamma y_\xi - x_\xi y_\gamma),\\
J &= x_\xi y_\eta z_\gamma + x_\gamma y_\xi z_\eta + x_\eta y_\gamma z_\xi - x_\xi y_\gamma z_\eta - x_\gamma y_\eta z_\xi - x_\eta y_\xi z_\gamma
\end{aligned}
\tag{3}
$$

and $S\ (\xi, \eta, \gamma)$ is the source term of the governing equation in $(\xi, \eta, \gamma)$ co-ordinates.

A staggered grid system as described in Reference 20 is used for the calculation. The scalar variables ($p, \rho, k, \varepsilon$, etc.) are located at the centres of the control volumes, whereas the velocity components are located on the control volume faces. Finite difference approximations to the conservation laws are obtained by taking the integral of equation (2) over the control volume and discretizing it, as done in Cartesian co-ordinates. The detailed implementation of the numerical algorithm is given in References 17 and 18.

Several choices of finite difference operators are available.[21,22] Besides using the so-called hybrid scheme[20] to approximate the convection terms, the second-order upwind scheme[21–24] is also used and the results are compared with those obtained with the hybrid scheme. As discussed in References 21–24, the second-order upwind scheme has been analysed and tested in the various one- and two-dimensional flow problems with good results being obtained. The present study is the first attempt to assess the performance of this scheme in the context of a three-dimensional turbulent flow. All other derivatives in the governing equations are discretized using the standard second-order central differencing scheme.

In the current formulation, the momentum equations are written in terms of the Cartesian velocity components, whereas the continuity equation uses the contravariant velocity components. This formulation has the advantage that the respective equations retain reasonably simple forms without a large number of additional terms. However, difficulties may appear when the grid lines turn ninety degrees from their original orientation, where the beneficial effects of the grid staggering are lost. As shown in Figure 4, for the grid staggering to be effective, the velocities on the control volume faces should be driven by the pressures at the main grid points on either side of the face, as at position (a). When the grid lines turn ninety degrees, as at position (b), the velocities on the control volume faces are no longer driven by the pressures stored at the main grid points on either side, but rather by the interpolated values at the corners of the control volume. Since the corner pressures are a six-point average of the pressures at the adjacent main grid points, any

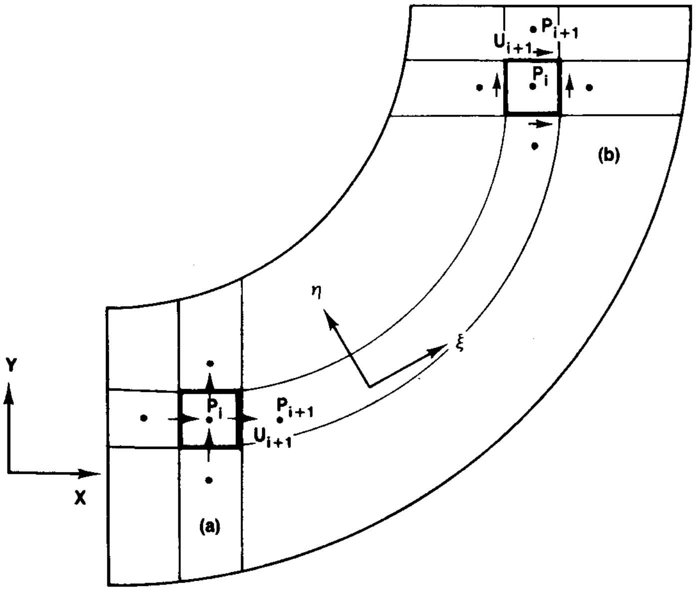

Figure 4. Effect of control volume orientation on the effectiveness of the grid staggering: (a) effective grid staggering ($\xi = x, \eta = y$); (b) ineffective grid staggering ($\xi = y, \eta = x$)

'chequerboard' pressure field that gives constant values for the corner pressures will be felt as a uniform pressure field by the momentum equations. The entire subject of pressure decoupling and the existence of chequerboard pressure fields has been described by several authors.[20,25]

A simple means of extracting a physically meaningful pressure field from a chequerboard pressure field, which is commonly adopted in many finite element procedures which use a non-staggered grid,[25] is to post-process the computed pressure field by a suitable averaging procedure. In the present formulation, six-point averaging is used to interpolate the pressure values at the main grid nodes to the corner points of the control volumes. These locations are precisely where the interpolated pressures appear naturally in the momentum equations when the grid lines turn ninety degrees. When the grid lines are aligned with the co-ordinate lines, this post-processing merely implies an additional smoothing of the pressure gradient consistent with that in the momentum equations, which does not degrade the numerical accuracy. Consequently, the post-processed pressure field appears physically realistic since it is essentially the pressure field that drives the discrete form of the momentum equations.

The solution procedure marches sequentially through the momentum, pressure correction, and other scalar equations (such as $k, \varepsilon$), with a maximum allowance being prescribed for updating each dependent variable. This sequential procedure is defined here as the outer iteration cycle. The discretized system of linear equations for each variable is also solved iteratively. This procedure is called the inner iteration step. It is found that the degree of convergence of the solution of the individual equations in the inner iterations can be very influential in affecting the overall rate of convergence of the outer iterations.

Initially, the linear equations were formulated and solved on a series of two-dimensional planes comprising the solution domain. Only one pass was made through the domain, to avoid the need to recompute the coefficients. During the course of this work, it was sometimes found that this original procedure did not converge to a steady-state solution. The mass residual failed to decay below about 10 per cent of the total flow rate, and the flow-field showed a persistent periodic oscillation of non-negligible magnitude as the iterations progressed. Later, it was discovered that the reason for this behaviour was that a single pass through the pressure correction equation did not give pressure corrections of sufficient accuracy to ensure that the corrected velocity field satisfied continuity closely enough. When the number of passes through the continuity equation was increased a more converged solution was attained.

The drawback to having to make multiple passes through a series of two-dimensional planes is that the coefficients must then be recomputed for each pass, which adds significantly to the computational cost. To avoid the need to recompute the coefficients, a new procedure was developed in which the coefficients were calculated and stored over the full three-dimensional domain. The resulting three-dimensional equations were solved by repeated sweeps of point- or line-SSOR to the desired level of convergence, which was taken to be when the total of all the residuals for the given equation fell below 10 per cent of its initial level.

For flows of meaningful Reynolds number, the pressure correction equation, which is Poisson-like[17] and hence inherently elliptic in nature, needed more iterative steps to converge than the momentum or scalar transport equations, which are convection dominated. Typical rates of convergence for the various equations are shown in Figure 5. The spectral radius of the momentum and scalar transport equations, measured as the ratio of the residuals summed over all of the nodal points between two successive inner iterations, was typically less than 0·1, when the point-SSOR method was used. The spectral radius of the pressure correction equation was generally found to be

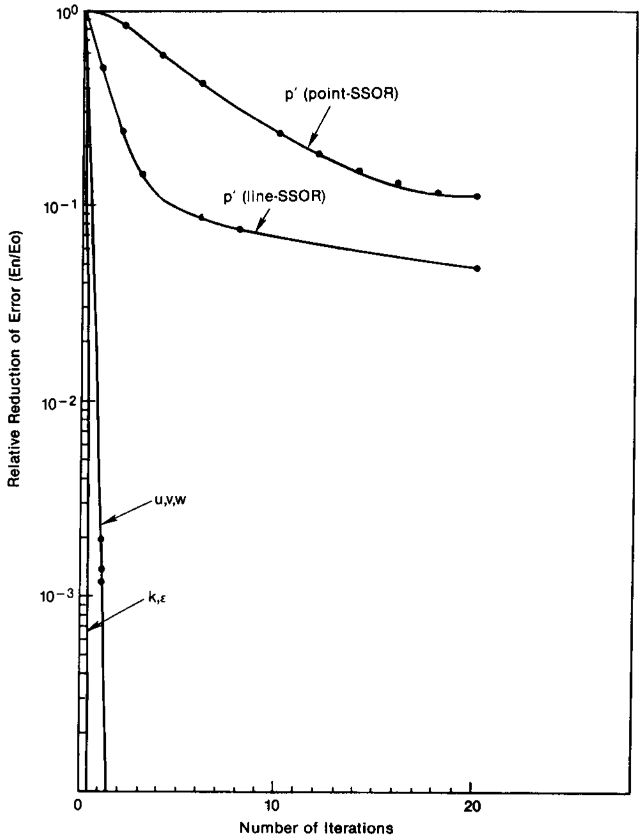

Figure 5. Reduction of error for the various equations

around 0·8 or higher for point-SSOR. Line-SSOR was found to provide substantially faster convergence than point-SSOR for the pressure correction equation, but the pressure correction equation still often needed an order of magnitude more iterative sweeps than the momentum and scalar transport equations to reach the same degree of convergence in the inner iteration step.

The improvement in the overall convergence rate that results from solving the linearized equations at each step to a suitably close convergence is demonstrated by the results shown in Figure 6. Here the decay of the mass residual is shown for both the old and new procedures as a

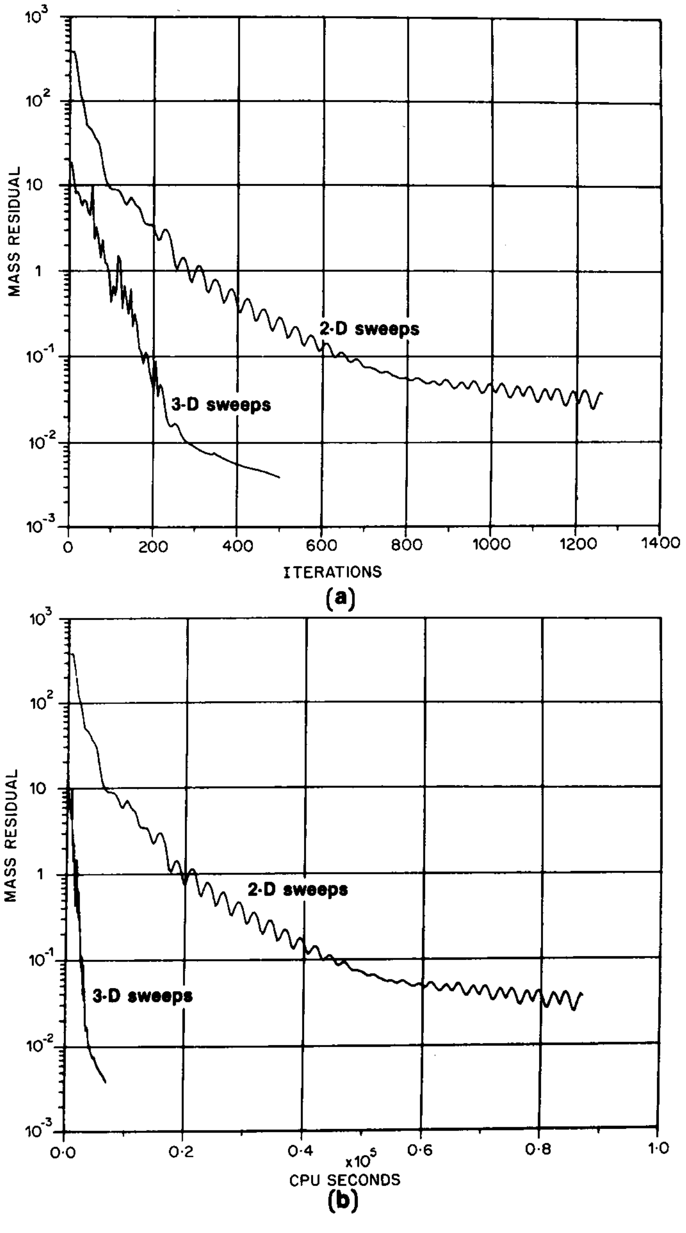

Figure 6. Comparison of the old and new algorithms: (a) normalized mass residual versus number of iterations; (b) normalized mass residual versus CPU time (FPS-164)

function of the number of outer iterations and the CPU time for a typical calculation. The saving in CPU time achieved by not having to recompute the coefficients within the inner iterations is obvious from the results, as the new procedure required ten times less computer time than the old procedure.

## DISCUSSION

A series of calculations was made for turbulent flow in a sample hydraulic turbine draft tube to study the resulting flow patterns and to investigate the effect swirl on the pressure recovery factor. First, the numerical performance of the solution algorithm is discussed. Then, a number of plots showing the resulting velocity vectors and pressure contours for both non-swirling inlet flow and strongly swirling inlet flow are presented, and the effect of inlet swirl on the pressure recovery factor is described. Finally, the effect of mesh refinement on the computed solution is discussed.

A non-orthogonal curvilinear mesh was generated for the draft tube geometry shown earlier in Figure 2. Two grid systems, one with 34 × 16 × 12 nodes and another with 50 × 30 × 22 nodes, are used and the results from them are compared. The grid distributions on some representative sections are shown in Figure 7, where the fine grid system is depicted.

The pressure recovery factor is known to be sensitive to the inlet axial flow profile and the inlet swirl.[2,6,9] In this work, the following definition of the pressure recovery factor $C_{\mathrm{pr}}$ was used:

$$C_{\mathrm{pr}} = \frac{\bar{P}_{\mathrm{out}} - \bar{P}_{\mathrm{in}}}{\frac{1}{2}\rho(\bar{U}_{\mathrm{in}}^2 + \bar{W}_{\mathrm{in}}^2)}. \tag{4}$$

Here $\bar{P}_{\mathrm{in}}$ and $\bar{P}_{\mathrm{out}}$ are the average static pressure at the inlet and outlet, respectively; $\rho$ is the fluid density, $\bar{U}_{\mathrm{in}}$ is the mean inlet velocity and $\bar{W}_{\mathrm{in}}$ is the mean inlet swirl velocity. The pressure recovery factor is a measure of how efficiently the draft tube converts excess kinetic energy in the fluid stream into a static pressure rise.

Experimental data on the actual inlet velocity profiles in a model draft tube showed that the inlet conditions could be reasonably approximated by a plug flow axial velocity profile with solid body rotation. The swirl can be characterized by the swirl ratio $S$, which is defined as the ratio of the maximum swirl velocity to the bulk axial velocity at the inlet. The Reynolds number for the flows

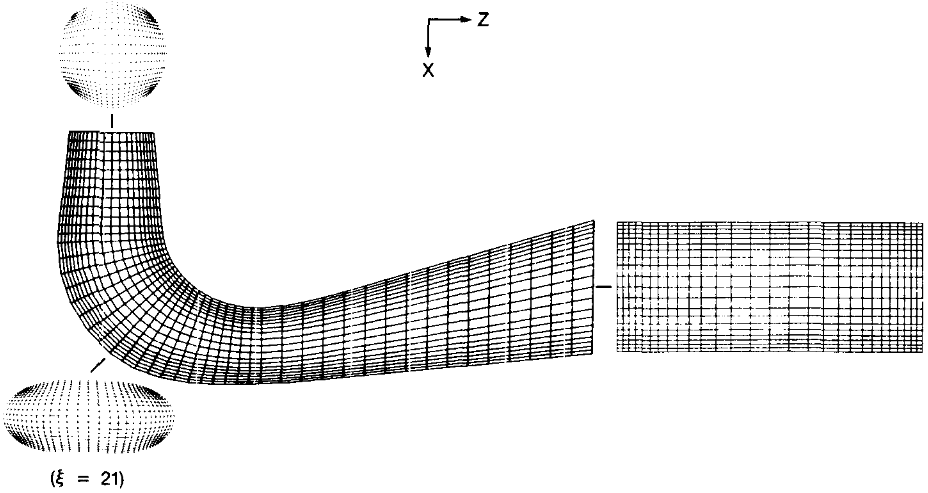

Figure 7. Grid system for tube calculation (50 × 30 × 22 grid)

investigated here was taken to be $10^6$. The swirl ratio $S$ was varied between 0 and 1·0. The test cases are summarized in Table I.

Figure 8 compares the convergence histories of the second-order upwind scheme on the fine and coarse grids for a representative case, $S = 0{\cdot}75$. Essentially, Figure 8 indicates that the number of iterations needed to yield the same degree of convergence increases no more than a factor of $\sqrt{N}$, where $N$ is the total number of grid points being employed. This result is as good as that reported for the two-dimensional cases.[26] Figure 9 compares the performances of the hybrid and second-order upwind schemes on the fine grid with $S = 0{\cdot}75$. The characteristics on the coarse grid as well as with different swirl ratios are similar to those in Figure 9. It is seen that the second-order upwind scheme requires slightly more iterations than the hybrid scheme to yield a comparable degree of convergence. However, the kinetic energy level of the results obtained by using the second-order upwind scheme is higher owing to smaller numerical dissipation effects.

In the following, the results calculated using the second-order upwind scheme on the fine grid system will be presented first in Figures 10–14. Other results will then be presented and compared. Figures 10–12 show the velocity field in the elbow region with $S = 0, 0{\cdot}75$ and 1·0, respectively. Several interesting features can be observed. First, for $S = 0$, it can be seen that on the mid-plane the maximum of the streamwise velocity first moves to the inner wall in the entrance of elbow region and then to the outer wall in the downstream region. These characteristics are consistent with those generally observed in a curved channel with a plug flow inlet profile (Reference 14, p. 52 References 27 and 28). By comparing the velocity directions in the side-wall region to those on the mid-plane, it is also clear that a double-eddy secondary flow pattern is present in Figure 10. It is noted that, as demonstrated in Reference 27, the flow characteristics in the elbow region are highly sensitive with respect to the change of inlet velocity profiles. Figure 11 shows that with the introduction of the inlet swirl, here $S = 0{\cdot}75$, on the mid-plane, the velocity vectors tend to have minimum magnitudes in the middle of the tube in the elbow. On the other hand, the velocity profile coming out of the elbow region is much more uniform than that with $S = 0$. By comparing the velocity directions on the mid-plane to those in the side-wall region, it is seen that the secondary recirculation becomes weaker as $S$ increases. Finally, in Figure 12 with $S = 1{\cdot}0$, the flow in the elbow region clearly bifurcates to the inner and outer walls and, as shown in Figure 12(c) in the $u$-velocity contour plots, a region of backflow start to appear in the middle.

Figure 13 shows the velocity vectors on the mid-plane of the flow region close to the exit. With no inlet swirl, the flow in the expansion region has a relatively low speed with a cellular type of

Table I. Test cases considered

| | | Coarse grid: 34 × 16 × 12 nodes | | Fine grid: 50 × 30 × 22 nodes | |
|---|---|---|---|---|---|
| Case number | Swirl ratio | Hybrid scheme | Second-order upwind scheme | Hybrid scheme | Second-order upwind scheme |
| 1 | 0 | C | C | C | C |
| 2 | 0·1 | C | — | — | — |
| 3 | 0·2 | C | — | — | — |
| 4 | 0·3 | C | C | C | C |
| 5 | 0·5 | C | C | C | C |
| 6 | 0·75 | C | C | C | C |
| 7 | 1·00 | — | — | C | C |

C: has been calculated
—: has not been calculated

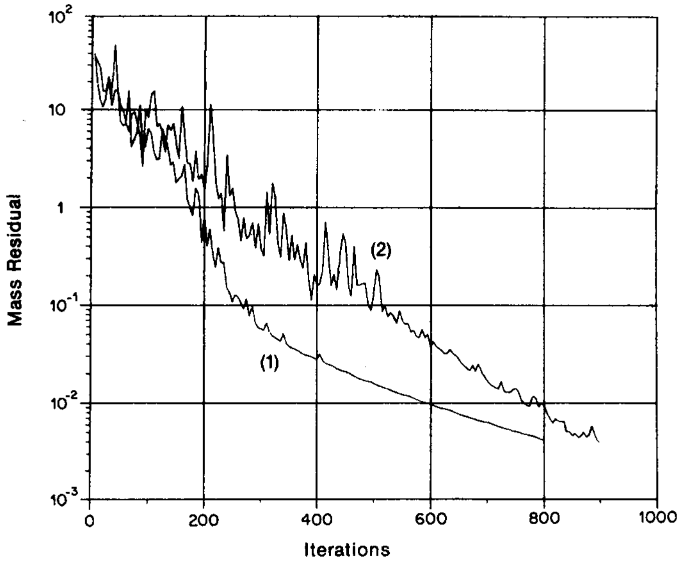

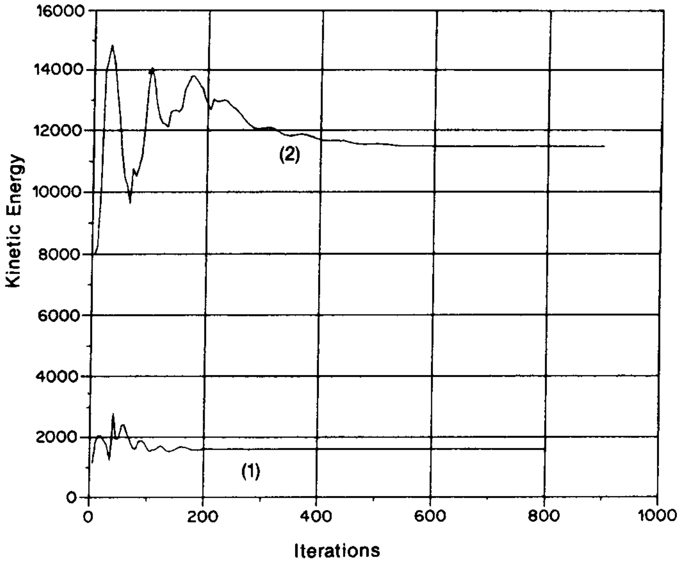

Figure 8. Convergence histories, second-order upwind scheme, $S = 0{\cdot}75$: (1) $34 \times 16 \times 12$ grid; (2) $50 \times 30 \times 22$ grid

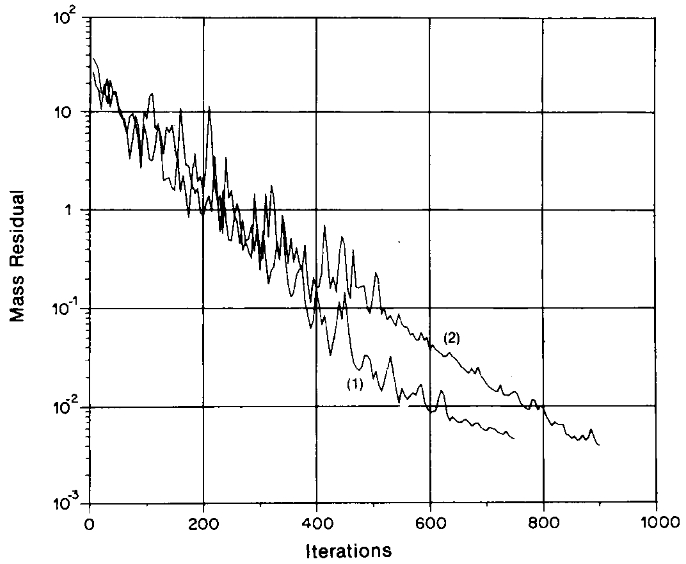

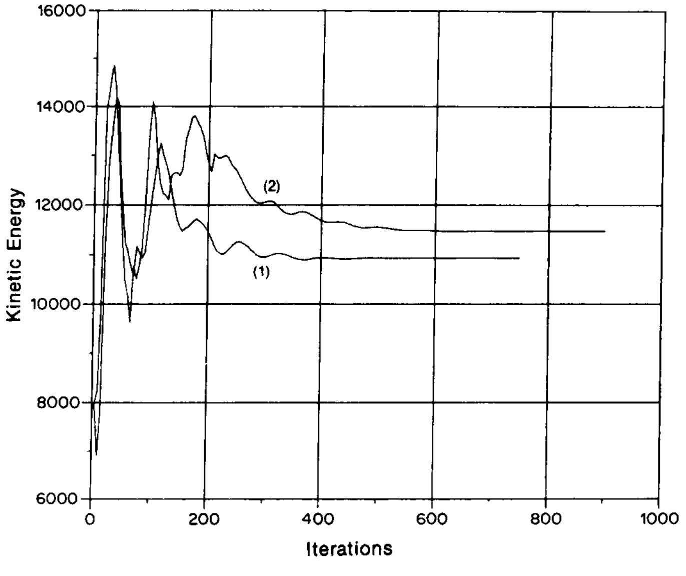

Figure 9. Convergence histories, $S = 0{\cdot}75$, $50 \times 30 \times 22$ grid: (1) hybrid scheme; (2) second-order upwind scheme

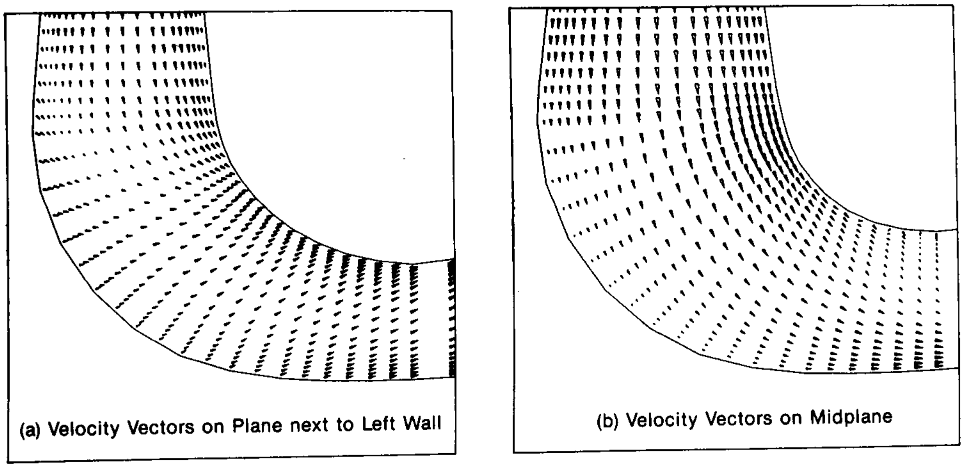
(a) Velocity Vectors on Plane next to Left Wall

(b) Velocity Vectors on Midplane

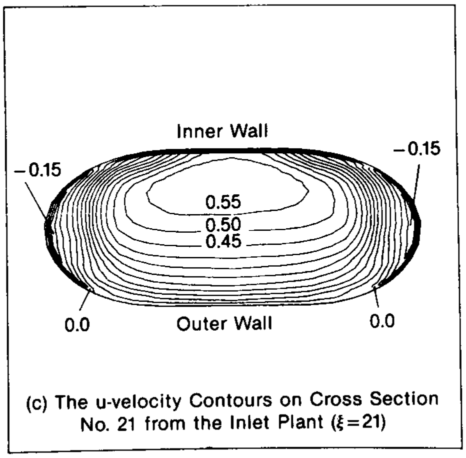

(c) The u-velocity Contours on Cross Section No. 21 from the Inlet Plant ($\xi=21$)

Figure 10. Flow field in the elbow region, 50 × 30 × 22 grid, second-order upwind scheme, $S = 0$

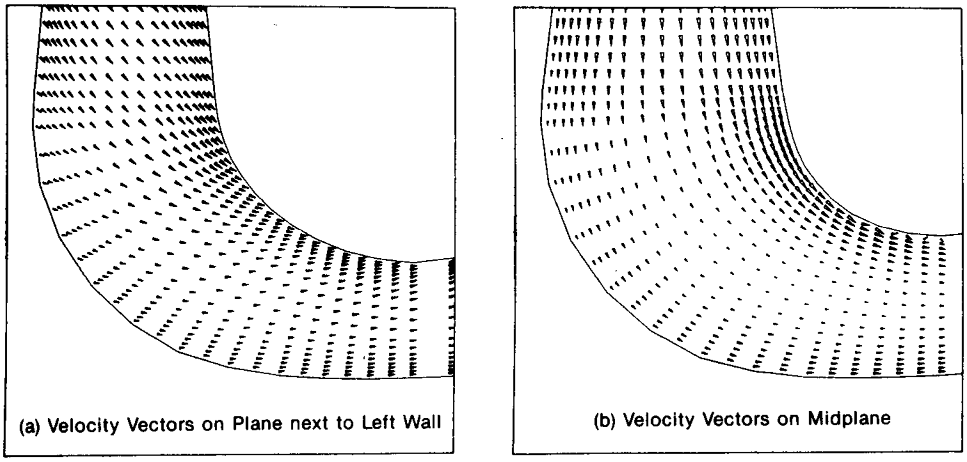

(a) Velocity Vectors on Plane next to Left Wall

(b) Velocity Vectors on Midplane

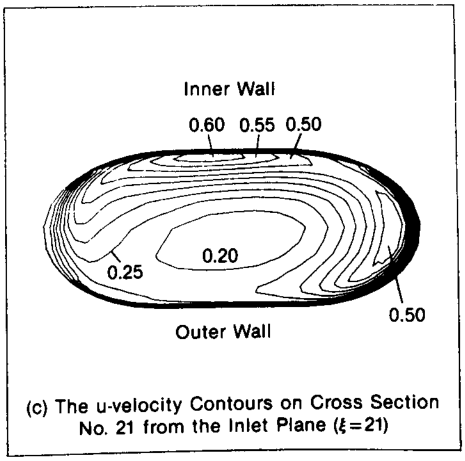

(c) The u-velocity Contours on Cross Section No. 21 from the Inlet Plane ($\xi=21$)

Figure 11. Flow field in the elbow region, 50 × 30 × 22 grid, second-order upwind scheme, $S = 0{\cdot}75$

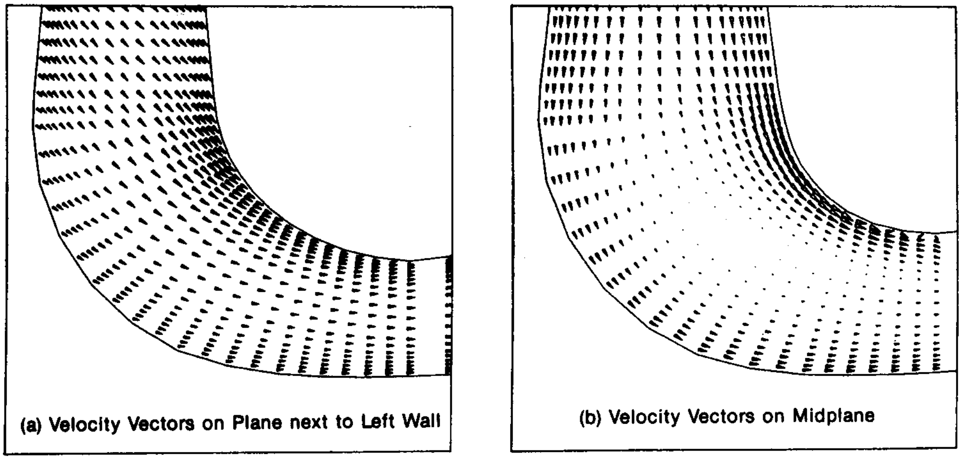

(a) Velocity Vectors on Plane next to Left Wall

(b) Velocity Vectors on Midplane

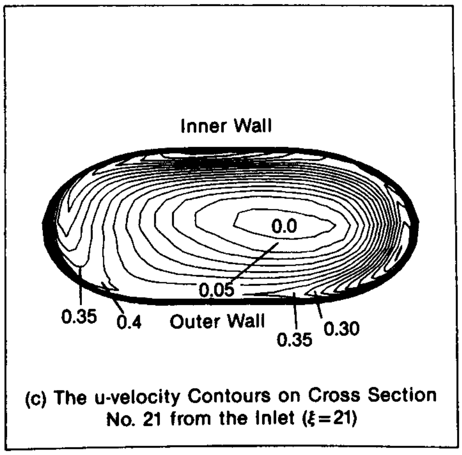

(c) The u-velocity Contours on Cross Section No. 21 from the Inlet ($\xi=21$)

Figure 12. Flow field in the elbow region, $50 \times 30 \times 22$ grid, second-order upwind scheme, $S = 1{\cdot}0$

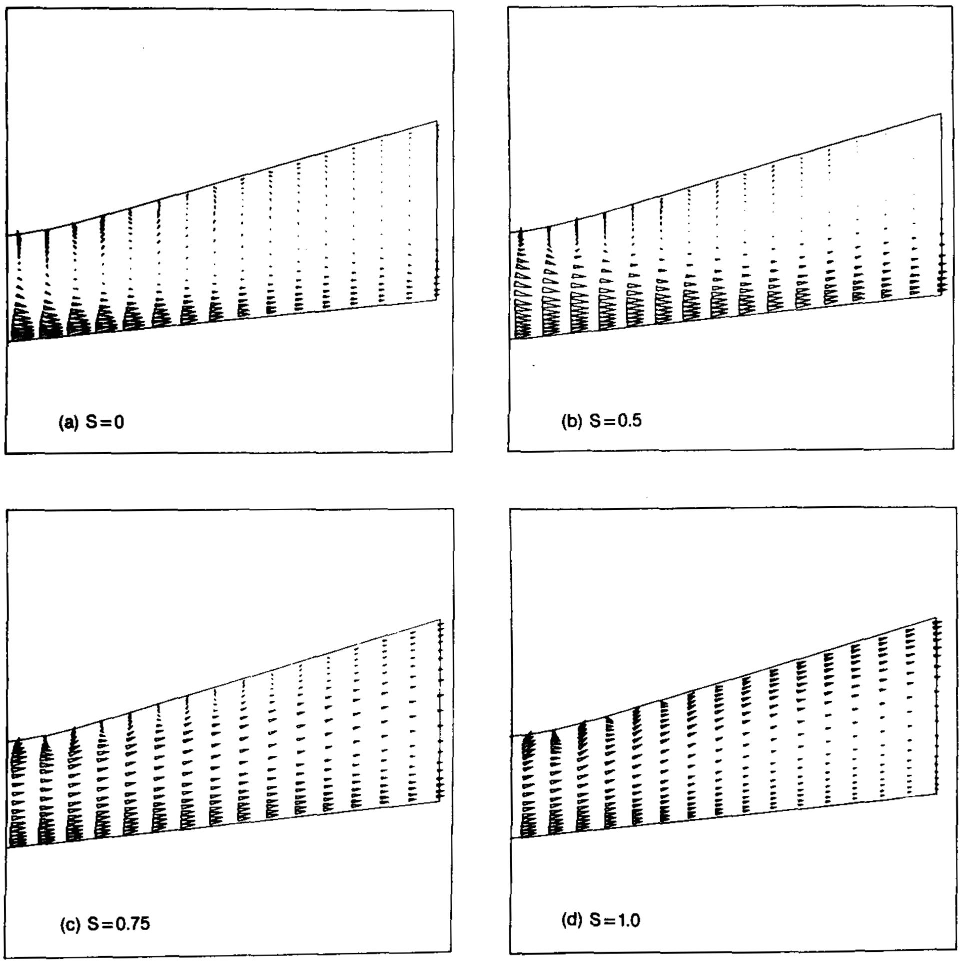

Figure 13. Velocity vectors on midplane of exit region, 50 × 30 × 22 grid, second-order upwind scheme

structure. The velocity profiles are highly non-uniform with backflow being present in the streamwise direction. With the introduction of inlet swirl, the streamwise backflows tend to disappear as $S$ increases. Figure 14 shows the static pressure contours on the whole mid-plane with four different values of $S$. The cellular structure in the expansion side is certainly very striking and closely mimics the velocity vectors shown in Figure 13. The effects of the inlet swirl can also be clearly seen from the curvature characteristics in the inlet region. For all of the cases considered here, the swirl essentially dies out before the flow passes through the elbow region.

The results obtained by using the hybrid scheme on the fine grid are qualitatively similar to those of the second-order upwind scheme except that the former generally shows the larger smearing effects of the hybrid scheme. The cellular flow structure obtained by using the hybrid scheme in the expansion side generally does not persist as far as that obtained with the second-order upwind scheme.Figure 15 shows the static pressure contours on the mid-plane for $S = 0{\cdot}75$ with the hybrid scheme being employed on the fine grid system. Figure 16 compares the velocity vectors in the elbow region obtained by using the two different finite difference operators, for the case of $S = 1{\cdot}0$ and the fine grid system. The extra numerical diffusion associated with the hybrid scheme makes

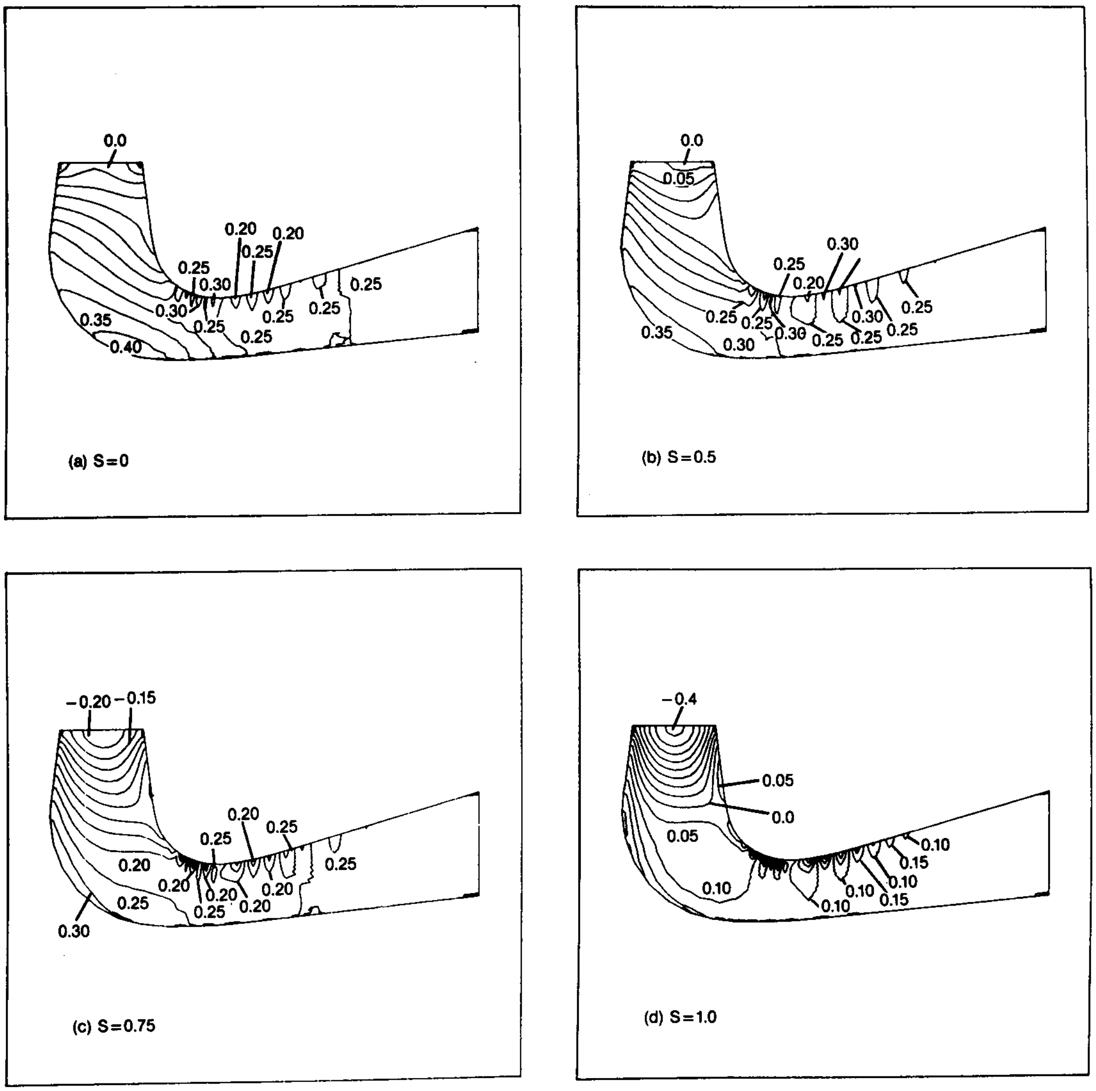

Figure 14. Static pressure contours on the mid-plane, 50 × 30 × 22 grid, second-order upwind scheme

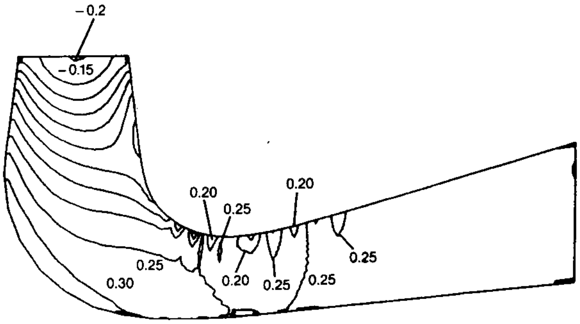

Figure 15. Static pressure contours on the mid-plane, 50 × 30 × 22 grid, hybrid scheme, $S = 0{\cdot}75$

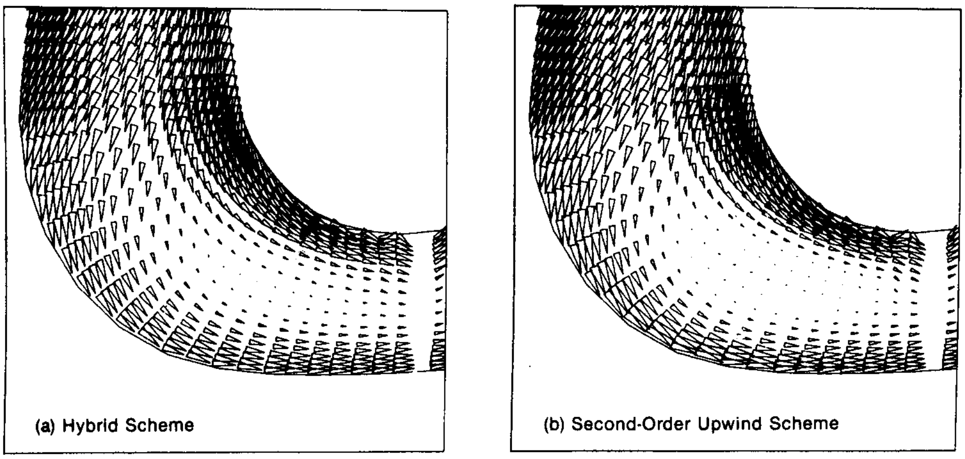

Figure 16. Comparison of the results for the velocity field in the elbow region obtained by using two finite difference operators: 50 x 30 x 22 grid, $S = 1{\cdot}0$; the plane shown is the tenth counted from the right end-wall

the velocity deficits in the middle flow region less pronounced. The larger region of streamwise recirculation predicted by the second-order upwind scheme is clearly visible.

It is interesting to note that, although the flow configurations are different, the effects of swirl observed here are generally consistent with those of Harvey[29] and So,[30] who found experimentally that, in a conical diffuser, a reversed flow region appears on the centre line when the inlet swirl is strong. Nevertheless, in the present study, the region where the streamwise backflow occurs, i.e. the elbow region, is unique to the present flow configuration.

Figure 17 compares the pressure recovery factors as a function of swirl ratio for the two schemes on the fine grid system. Qualitatively, both results show that the pressure recovery factors increase with the swirl ratio up to some point, and then drop off. It is interesting to note that with less numerical dissipation being added, the pressure recovery factors for low swirl ratios predicted by using the second-order upwind scheme are smaller than those using the hybrid scheme. A possible reason is that, with smaller numerical diffusion, the second-order upwind scheme predicts a stronger stalling characteristic with more noticeable cellular structure for the flows with low swirl ratio. As the inlet swirl becomes stronger, up to $S = 0{\cdot}75$, the velocity fields become more uniform, especially in the downstream area expansion region, and hence the pressure recovery factor predicted by the second-order upwind scheme, with the help of smaller numerical dissipation, is able to show a higher value.

For the high inlet swirl, $S = 1{\cdot}0$, the flow field starts to bifurcate in the elbow region and streamwise backflows appear. This phenomenon causes a noticeable drop in terms of the overall pressure revovery factor. Figure 18 compares the outflow ($w$) velocity profiles at the centre of the exit plane, drawn from left to right end-walls, as predicted by the two finite difference operators on the fine grid system. Figure 18 shows a tendency of increasing non-uniformity of the exit velocity profile with increasing inlet swirl. In all cases, the two predictions are in general consistent with each other, except that the steeper velocity gradients yielded by the use of the second-order upwind scheme are shown in the wall region. In summary, for all of the results compared on the fine grid system, there exists reasonable agreement between the predictions yielded by the two finite difference operators with some illuminating flow structures being revealed.

Figure 19 compares the predictions of the pressure recovery factors yielded by the two finite difference operators on the coarse grid system with 34 x 16 x 12 nodes. Again the two predictions

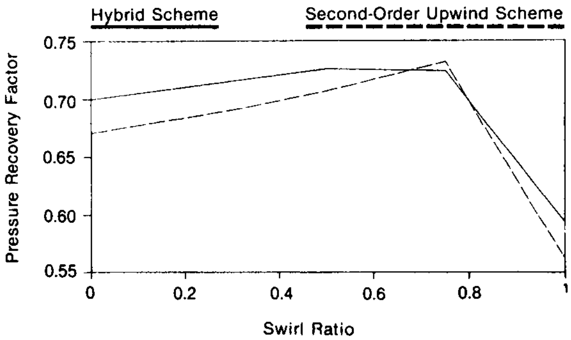

Figure 17. Pressure recovery factor vs. swirl ratio, fine grid: ——— hybrid scheme; – – – – second-order hybrid scheme

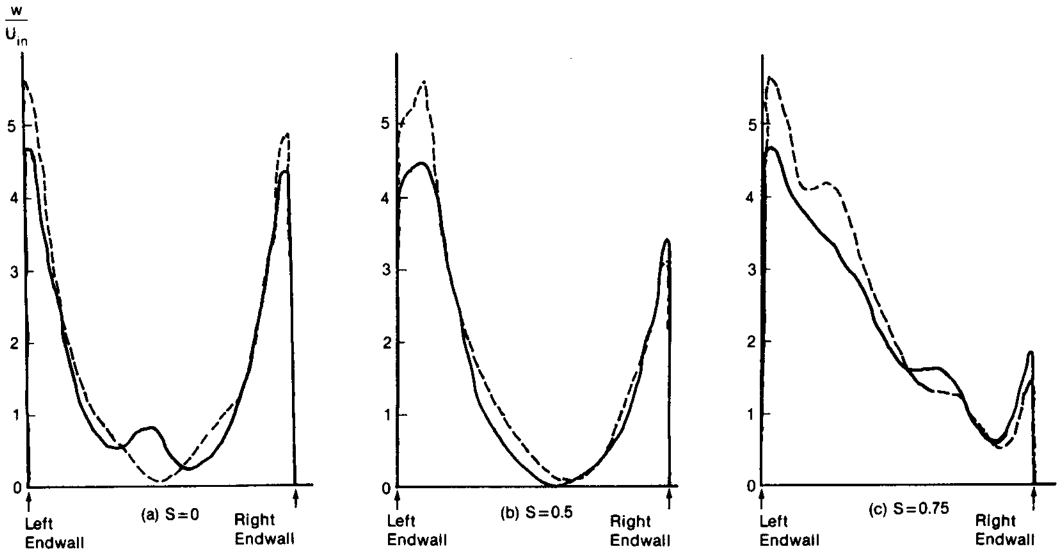

Figure 18. Comparison of outflow (*w*) velocity profiles at the centre of the exit (drawn from left to right end-walls), 50 x 30 x 22 grid; ——— hybrid scheme; – – – – second-order upwind scheme

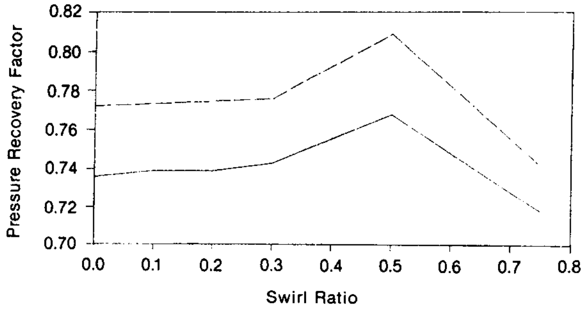

Figure 19. Pressure recovery factor vs. swirl ratio: ——— hybrid 34 x 16 x 12 grid; – – – – second-order hybrid, 34 x 16 x 12 grid

show an overall agreement in terms of the qualitative behaviours. However, on the coarse grid, the pressure recovery factors yielded by the use of the second-order upwind scheme are higher than those of the hybrid scheme. The reason is that on a grid this coarse, neither scheme under study was able to predict a noticeable stalling characteristic in the downstream expansion region, even for the no-swirl case. Figure 20 compares the velocity fields calculated with the two different finite difference operators on the coarse grid. Although there are some quantitative differences between the two predictions, the flow characteristics calculated on the coarse grid with either finite difference operator are generally smeared out and do not show the clear cellular structure in the expansion region that is observed in the fine grid solutions. Figure 21 compares the outflow velocity profiles predicted on the coarse grid systems. On the coarse grid, whereas the second-order upwind scheme predicts a somewhat more noticeable non-uniformity of the exit velocity profiles with the increasing inlet swirl, it does not produce good agreement with the profiles calculated on the fine grid with the same finite difference operator. Based on the results presented, it is clear that a combination of a good finite difference operator and a good grid distribution is necessary to yield a satisfactory prediction.

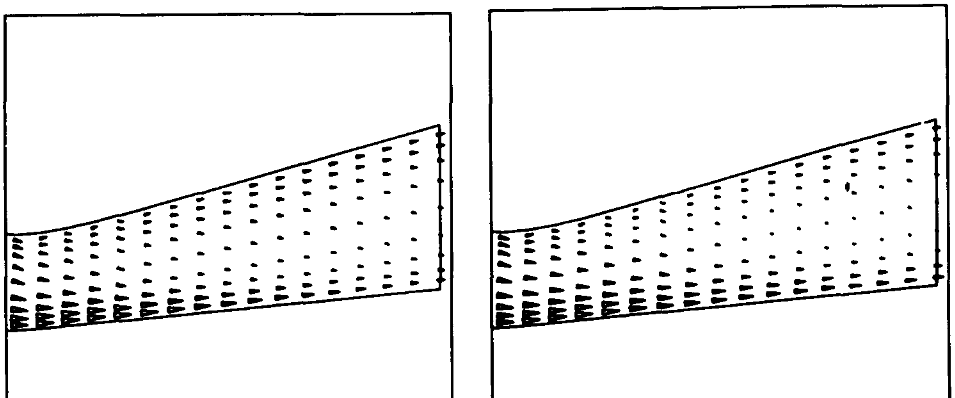

(a) Second-Order Upwind Scheme, S=0

(b) Hybrid Scheme, S=0

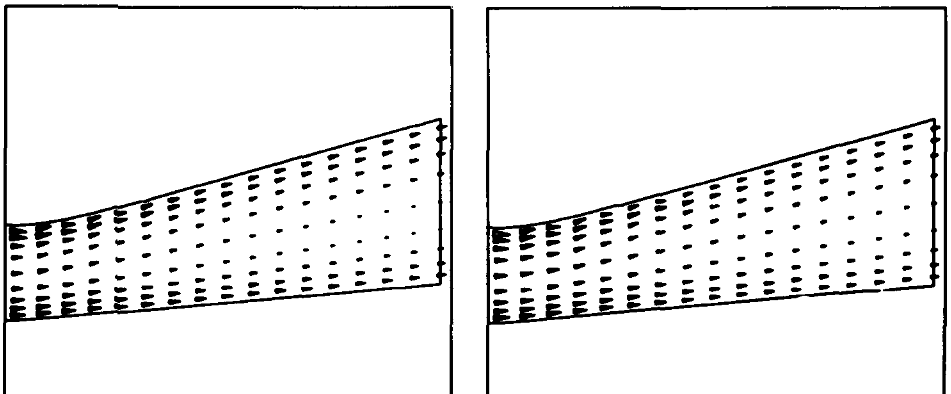

(c) Second-Order Upwind Scheme, S=0.75

(d) Hybrid Scheme, S=0.75

Figure 20. Velocity vectors on the mid-plane of the exit region, 34 × 16 × 12 grid

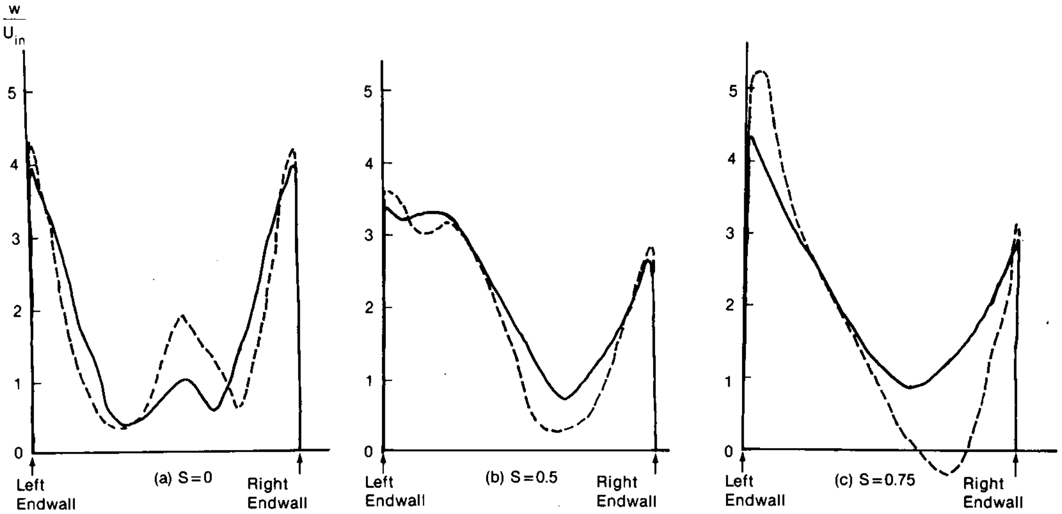

Figure 21. Comparison of outflow ($w$) velocity profiles at the centre of the exit (drawn from left to right end-walls), $34 \times 16 \times 12$ grid: ——— hybrid scheme; ——— second-order upwind scheme

## SUMMARY AND CONCLUDING REMARKS

A series of three-dimensional elliptic flow calculations have been conducted for a curved hydraulic turbine draft tube. Various numerical issues including the solution procedure for the various equations and a method for eliminating unphysical oscillations in the computed pressure field have been discussed. The effects of the inlet swirl ratio on the flow field and the pressure recovery factor have been investigated. Two finite difference operators, i.e. the hybrid and second-order upwind scheme, have been compared and two grid systems adopted.

The addition of inlet swirl shows a strong influence on the overall flow structure. With an increase in inlet swirl, it is found that not only can the stalling characteristics in the downstream region be effectively eliminated, but also that the flows in the elbow region show markedly different behaviour. The maximum streamwise velocity in the elbow region shows a marked shift according to the strength of the inlet swirl and hence can affect the overall pressure recovery factors noticeably. The exit velocity profiles also show an increasing non-uniformity as the inlet swirl increases. It is found that many of the salient features observed on the fine grid system are smeared out on the coarse grid system.

As to the finite difference operators, although the general trends predicted by both the operators are in agreement, the quantitative values as well as some finer flow structures can differ. Overall, a detailed account has been given in the analysis of this complicated flow problem and some very illuminating characteristics have been observed.

## ACKNOWLEDGEMENTS

Since thanks are due to Mr. Thi C. Vu and Mr. Andre Couture of Dominion Engineering Works Limited, Montreal, Quebec, Canada, who provided us with the draft tube geometry and the coarse body-fitted mesh, and the experimental information on the inlet velocity profiles in a model draft tube. Thanks are also to Ms. Carol Cowsert and Ms. Virginia Warner for their excellent typing.

## REFERENCES

1. R. W. Fox and S. J. Kline, 'Flow regimes in curved subsonic diffusers', *J. Basic Engineering*, 303–316 (1962).
2. D. Japikse, *Turbomachinery Diffuser Design Technology*, Concepts ETI, Inc., Norwich, Vermont, 1984.
3. M. S. Jubin, *Draft Tube of Hydroelectric Stations*, Enerjiya Press, Moscow, 1970, Chapter 5.
4. R. W. Fox and S. J. Kline, 'Flow regime data and design methods for curved subsonic diffusers', Stanford University, Dept. of Mechanical Engineering, PD-6, 1960.
5. C. J. Sagi and J. P. Johnston, 'The design and performance of two-dimensional, curved diffusers. Part I: exposition of method', and 'Part II: experiment, evaluation of method, and conclusions', *Journal of Basic Engineering*, **89, (4)**, 715–732 (1967).
6. A. T. McDonald, R. W. Fox and R. V. Van Dewoestine, 'Effects of swirling inlet flow on pressure recovery in conical diffusers', *AIAA Journal*, **9**, (10), 2014–2018 (1971).
7. S. V. Patankar, V. S. Pratap and D. B. Spalding, 'Prediction of turbulent flow in curved pipes', *J. Fluid Mech.*, **67**, 583 (1975).
8. W. R. Briley and H. McDonald, 'Three-dimensional viscous flows with large secondary velocity', *J. Fluid Mech.*, **144,** 47–77 (1984).
9. C. Hah, 'Calculation of various diffuser flows with inlet swirl and inlet distortion effects', *AIAA Journal*, **21,** (8), 1127–1133 (1983).
10. M. Reggio and P. Camarero, 'A three-dimensional solution method for turbomachinery analysis', *1985 ASME Winter Annual Meeting*, 153–162 (1985).
11. W. Shyy, 'A numerical study of annular dump diffuser flows', *Comput. Meths. Appl. Mech. Eng.*, **52,** 47–65 (1985).
12. W. Shyy, 'Numerical outflow boundary condition for Navier–Stokes flow calculation by a line iterative method', *AIAA J.*, **23,** 1847–1848 (1985).
13. B. E. Launder and D. B. Spalding, 'The numerical calculation of turbulent flows', *Comput. Meths. Appl. Mech. Eng.*, **3,** 269–289 (1974).
14. W. Rodi, *Turbulence Models and their Applications in Hydraulics*, IAHR Section on Fundamentals of Division II: Experimental and Mathematical Fluid Dynamics, Delft, The Netherlands, 1980.
15. D. G. Lilley, 'Swirling flows in typical combustor geometries', *AIAA Paper No. 85–0184*, 1985.
16. H. Iacovides and B. E. Launder, 'ASM predictions of turbulent momentum and heat transfer in coils and U-bends', in C. Taylor *et al.* (eds), *Numerical Methods in Laminar and Turbulent Flows, Part 2*, Pineridge Press, Swansea, U.K., 1985, pp. 1023–1045.
17. W. Shyy, S. S. Tong and S. M. Correa, 'Numerical recirculating flow calculation using a body-fitted coordinate system', *Numer. Heat Trans.*, **8,** 99–113 (1985).
18. M. E. Braaten and W. Shyy, 'A study of recirculating flow computation using body-fitted coordinates: consistency aspects and mesh skewness', *Numer. Heat Trans.*, **9,** 559–574 (1986).
19. M. Vinokur, 'Conservative equations of gas dynamics in curvilinear co-ordinate systems', *J. Comput. Phys.*, **14,** 105–125 (1974).
20. S. V. Patankar, *Numerical Heat Transfer and Fluid Flow*, McGraw-Hill, New York, 1980.
21. W. Shyy, 'A study of finite difference approximations to steady-state, convection dominated flow problems', *J. Comput. Phys.*, **57,** 415–438 (1985).
22. W. Shyy and S. M. Correa, 'A systematic comparison of several numerical schemes for complex flow calculations', *AIAA Paper No. 85–0440*, 1985.
23. W. Shyy and T. C. Vu, 'A numerical study of incompressible Navier–Stokes flow through rectilinear and radial cascade of turbine blades', *Int. J. Comput. Mech.* (in press).
24. A. Plotkin and R. Mei, 'Navier–Stokes solutions for some laminar incompressible flows with separation in forward facing step', *AIAA Paper No. 86–0110*, 1986, also *AIAA Journal*, **24,** 1106–1111 (1986).
25. R. L. Sani, P. M. Gresho, R. L. Lee and D. F. Griffiths, 'The cause and cure (?) of the spurious pressures generated by certain FEM solutions of the incompressible Navier–Stokes equations', *Int. j. numer. methods fluids*, **1,** 17–43, 171–204 (1981).
26. M. E. Braaten and W. Shyy, 'Comparison of iterative and direct solution methods for viscous flow calculations in body-fitted coordinates', *Int. j. numer. methods fluids*, **6,** 325–349 (1986).
27. D. E. Olson and B. Snyder, 'The upstream scale of flow development in curved circular pipe', *J. Fluid Mech.*, **150,** 139–158 (1985).
28. D. Kwak, J. L. C. Chang, S. P. Shanks and S. R. Chakravarthy, 'An incompressible Navier–Stokes flow solver in three-dimensional curvilinear coordinate system using primitive variables', *AIAA Paper No. 84–0253*, Reno, NV, 1984.
29. J. K. Harvey, 'Some observations of the vortex breakdown phenomenon', *J. Fluid Mech.*, **14,** 585–592 (1962).
30. K. L. So, 'Vortex phenomena in a conical diffuser', *AIAA Journal*, **5,** 1072–1078 (1967).